

Horizontal flows concurrent with an X2.2 flare in active region NOAA 11158

L. Beauregard^{1,2}, M. Verma², and C. Denker^{2,*}

¹ McGill University, Department of Physics, 845 Sherbrooke St. W., Montreal, Quebec, Canada H3A 2T5

² Leibniz-Institut für Astrophysik Potsdam, An der Sternwarte 16, 14482 Potsdam, Germany

Received 2011 Sep 5, accepted 2012 Jan 9

Published online 2012 xxx

Key words Sun: activity – Sun: flares – Sun: magnetic fields – Sun: photosphere – sunspots – methods: data analysis

Horizontal proper motions were measured with local correlation tracking (LCT) techniques in active region NOAA 11158 on 2011 February 15 at a time when a major (X2.2) solar flare occurred. The measurements are based on continuum images and magnetograms of the *Helioseismic and Magnetic Imager* on board the *Solar Dynamics Observatory*. The observed shear flows along the polarity inversion line were rather weak (a few 100 m s⁻¹). The counter-streaming region shifted toward the north after the flare. A small circular area with flow speeds of up to 1.2 km s⁻¹ appeared after the flare near a region of rapid penumbral decay. The LCT signal in this region was provided by small-scale photospheric brightenings, which were associated with fast traveling moving magnetic features. Umbral strengthening and rapid penumbral decay was observed after the flare. Both phenomena were closely tied to kernels of white-light flare emission. The white-light flare only lasted for about 15 min and peaked 4 min earlier than the X-ray flux. In comparison to other major flares, the X2.2 flare in active region NOAA 11158 only produced diminutive photospheric signatures.

© 2012 WILEY-VCH Verlag GmbH & Co. KGaA, Weinheim

1 Introduction

Major solar flares have a variety of photospheric signatures, e.g., rapid and permanent changes of the magnetic field resulting in an increase of the transverse field and magnetic shear (Wang et al. 2002), penumbral decay and strengthening of umbral areas because initially inclined penumbral field lines become more vertical (Liu et al. 2005), coherent lateral displacement of penumbral filaments (Gosain, Venkatakrishnan, & Tiwari 2009), elongated magnetic structures along the polarity inversion line (PIL) (Wang et al. 2008; Zirin & Wang 1993), and changes of the vector magnetic field around the PIL on spatial scales below one second of arc (Kubo et al. 2007). The statistical significance of such photospheric changes associated with major flares was demonstrated in the work of Sudol & Harvey (2005).

Battaglia & Kontar (2011) presented a comparison of the height dependence of flare emission. Hard X-rays originate from 0.7 to 1.8 Mm above the photosphere, whereas EUV radiation is produced in the top layers of the chromosphere at about 3.0 Mm above the photosphere. Emission in the optical range covers the intermediate range from 1.5 to 3.0 Mm and was measured with the *Helioseismic and Magnetic Imager* (HMI) on board the *Solar Dynamics Observatory* (SDO) in the continuum near the Fe I $\lambda 617.3$ nm line. In contrast, observations by Xu et al. (2004) in the near-infrared at 1.6 μ m, i.e., at the opacity minimum, indicate that deep photospheric layers can exhibit emission asso-

ciated with flares as well. First spectroscopic observations with HMI of a M2.0 white-light flare on 2010 June 12 were reported by Martínez Oliveros et al. (2011), who noticed that the entire Fe I line profile was shifted towards the blue. However, interpreting sparsely sampled spectral data during flares (transients in magnetograms or Doppler maps) will not lead to conclusive results without detailed knowledge of instrument characteristics, data processing pipelines, and spectral line formation (cf., Maurya, Reddy & Ambastha 2011). Blue-shifted velocities of up to 1 km s⁻¹ were also identified as a common precursor of flares in the early work of Harvey & Harvey (1976). Hints that horizontal shear motions are important for the build-up of magnetic stress in flare-productive active regions were likewise presented by Harvey & Harvey (1976). The role of shear flows as drivers for magnetic reconnection was recently discussed by Yurchyshyn et al. (2006) and Liu et al. (2010) in the context of the tether-cutting model (Moore et al. 2001).

New telescopes with advanced post-focus instruments and novel data analysis techniques made it possible to study such shear motions in more detail. Using local correlation tracking (LCT, November & Simon 1988), Yang et al. (2004) measured shear flows with horizontal speeds of up to 1.6 km s⁻¹ on both sides of the PIL. Such head-on flows were separated by less than one second of arc. The well-defined regions of elevated flow speed showed a good correlation with kernels of white-light emission of an X10 flare – both in the visible and near-infrared continua. The height dependence of horizontal (shear) flows in active region NOAA 10486 was described by Deng et al. (2006).

* Corresponding author: e-mail: cdenker@aip.de

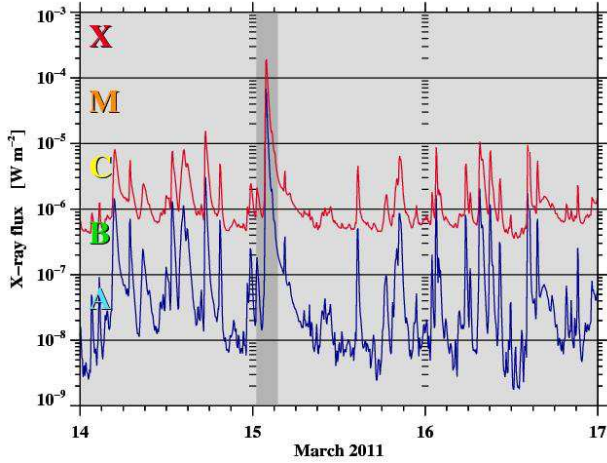


Fig. 1 GOES 15 X-ray flux (5-minute data) obtained during the time period from 2011 February 14–16 in the 0.1–0.8 nm (*top*) and 0.05–0.4 nm (*bottom*) energy channels. The shaded region indicates a time interval of three hours centered on the peak time (01:56 UT) of the X2.2 flare in active region NOAA 11158.

Shear flows are not limited to flare-prolific regions but are also encountered in quieter settings (Denker et al. 2007). Ultimately, the magnetic field topology and the interaction of magnetic fields and plasma motions has to be considered to decide, if shear flows contribute to the build-up of free magnetic energy or lead to more potential magnetic field configurations. Finally, based on data of the *Hinode* mission, Tan et al. (2009) provided crucial links between photospheric signatures of major flares and horizontal shear flows.

In Verma & Denker (2011), we developed a LCT algorithm for bulk-processing of *Hinode* G-band images. This work also includes references to alternative methods for measuring horizontal proper motions, e.g., differential affine velocity estimator (DAVE, Schuck 2006), non-linear affine velocity estimator (NAVE, Chae & Sakurai 2008), and ball-tracking (Potts, Barrett, & Diver 2004). We refer to Welsch et al. (2007) for an in-depth comparison of the various techniques to track horizontal proper motions. In this brief research note, we adapted the code of Verma & Denker (2011) to SDO/HMI continuum images. The X2.2 flare of 2011 February 15 was chosen as a promising target to search for alterations of the horizontal flow field after a major solar flare. The three-dimensional magnetic field topology of active region NOAA 11158 (observations and MHD modeling), coronal emission structures, and the eruptive events associated with the X2.2 flare (coronal mass ejection, EIT wave, and coronal front) are meticulously described and explained in Schrijver et al. (2011), so that we focus only on the photospheric signatures of the flare.

2 Observations

Active region NOAA 11158 began its disk passage on 2011 February 11 when it was still classified as a β -region. Besides the X2.2 flare, active region NOAA 11158 produced

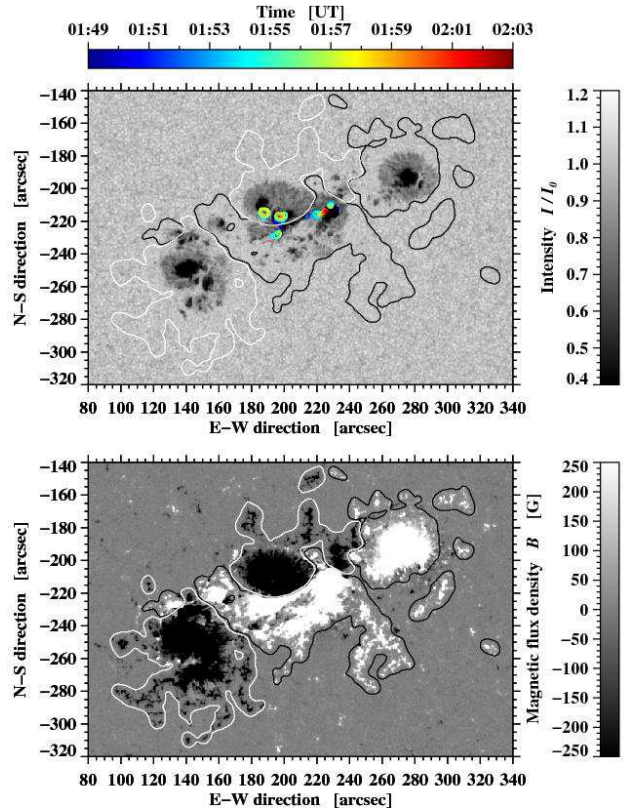


Fig. 2 Limb-darkening corrected continuum image (*top*) and magnetogram (*bottom*) of active region NOAA 11158, which were observed at 01:33 UT just before the onset of the flare. The black and white contour lines enclose strong (above/below ± 10 G) positive and negative flux concentrations, respectively. Strong PILs exist in regions where the contour lines overlap. The color-coded contour lines indicate kernels of white-light flare emission at different times. The axes are labeled in heliographic coordinates.

56 C-class flares and five M-class flares including two M6.6 events on February 13 and 18. The impulsive phase of the X2.2 flare started at 01:33 UT on 2011 February 15. This time was chosen as a reference for the subsequent data analysis. We divided the dataset into three parts: the 1-hour pre- and post-flare periods (00:33–01:33 UT and 02:18–03:18 UT) and the intervening 45-minute period covered by the flare. We assume that data outside of the flare period is unaffected by flare emissions. The X-ray flux measured by the *Geostationary Operational Environmental Satellite* (GOES) is shown in Fig. 1 for a three-day period centered on the major flare. The gray bar indicates the three-hour observing period.

This study is based on HMI continuum images and line-of-sight magnetograms. The instrument characteristics are presented in a series of articles: Wachter et al. (2011) give a detailed account of the image quality as measured during the ground calibration of the instrument. The characteristics of the optical filter system are laid out in Couvidat et al. (2011), who also discuss them in the context of the Fe I $\lambda 617.3$ nm line, which was chosen as the most suitable spectral line for HMI observations. Finally, polarization cal-

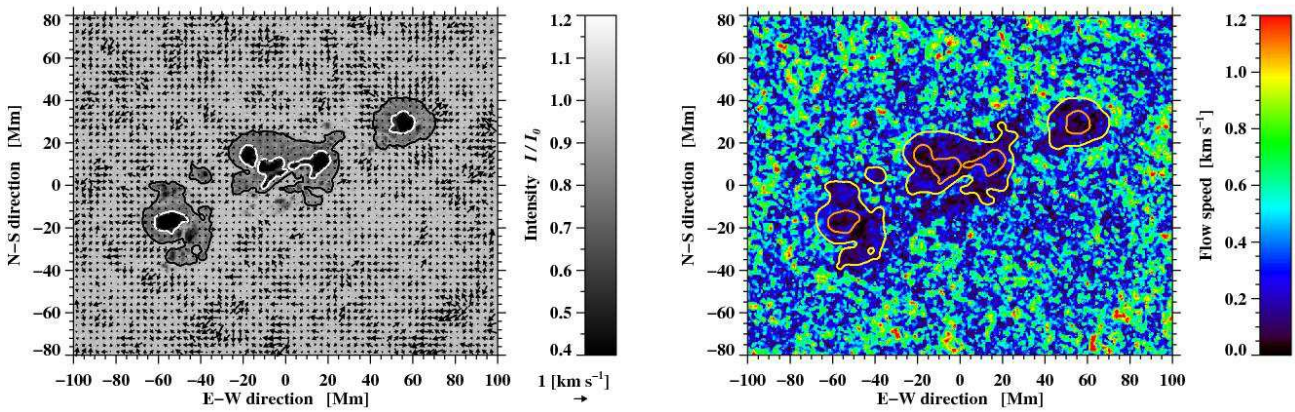


Fig. 3 Horizontal proper motions in active region NOAA 11158 during the pre-flare phase (00:33–01:33 UT). Arrows indicating magnitude and direction of the flow field are superposed on an average pre-flare continuum image (*left*). The arrow in the lower right corner corresponds to a flow speed of 1 km s^{-1} . The flow speed (*right*) is given according to the scale on the right to visualize the fine structure of the proper motions. The contour lines represent the granulation/penumbra and penumbra/umbra boundaries. The flow maps have been corrected for geometric foreshortening. The coordinates are given with respect to the center of the ROI.

ibration is described in Schou et al. (2010). Since detailed information is available, we only present a brief account of the observing characteristics relevant to our study.

HMI utilizes a 14-cm telescope ($F/37.4$). The diffraction limit at $\text{Fe I } \lambda 617.3 \text{ nm}$ is $\alpha = \lambda/D = 0.9'' \text{ pixel}^{-1}$. Thus, the data is slightly undersampled with an image scale of $0.5'' \text{ pixel}^{-1}$. The Fe I line is sampled at six line positions covering a range of $\lambda_0 \pm 17.5 \text{ pm}$. Full-disk data have a size of 4096×4096 pixels. Data are captured with a 45 s cadence resulting in 240 images and magnetograms during the period from 00:30 to 03:30 UT. A region-of-interest (ROI) with a size of $260'' \times 180''$ (see Fig. 2) was extracted from the full-disk data for further data analysis. The continuum images were corrected for the center-to-limb variation (see Denker et al. 1999) to facilitate feature recognition using thresholding techniques. The black and white contour lines in Fig. 2 were computed using a 10 G threshold for the smoothed magnetogram (Gaussian with a FWHM of 2 Mm). Locations, where the black and white contour lines overlap, indicate strong PILs, most prominently, the east-west oriented, flaring PIL in the center of the ROI.

The photospheric continuum emission of the X2.2 flare is difficult to measure. The peak contrast of the white-light flare kernels is less than a few percent of the local intensity contrast. Average values are even lower. For this reason, the quiet Sun intensity contrast of about 3.5% is sufficient to obfuscate the faint flare emission. Using Gaussian smoothing (FWHM of 2.0 Mm), division by a 30-minute running average, and a local intensity contrast of 5% as a threshold, we could determine contours of the flare kernels for about 15 min starting at 01:49 UT. Early flare emissions are color-coded from dark to light blue in the top panel of Fig. 2 and the left and middle columns of Fig. 4, whereas lighter to darker gradations of red outline later stages of the flare. The influence of the temporal interpolation function on HMI continuum images is discussed in Martínez Oliveros et al.

(2011). Since we are focussing on excess emission, side effects of the helioseismic interpolation scheme such as an apparent “black-light” flare precursor can be neglected.

The LCT algorithm is an adaptation of the code described in Verma & Denker (2011), who provide a detailed account of how to choose LCT input parameters and how that choice will affect the outcome of the LCT procedure. HMI continuum images are corrected for limb darkening and geometrical foreshortening. They are resampled on an equidistant grid with a spacing of 320 km. The local cross-correlations are computed over image tiles of 16×16 pixels ($5 \text{ Mm} \times 5 \text{ Mm}$). A Gaussian with a FWHM of 6.25 pixels (2 Mm) is used both as a weighting function and a high-pass filter. The cadence for correlating image pairs is $\Delta t = 90 \text{ s}$ and individual flow maps are average over $\Delta T = 1 \text{ h}$. Horizontal flow maps based on 80 continuum images were computed for the pre- and post-flare episodes. The flow field just before the onset of the flare is depicted in Fig. 3.

3 Results

Active region NOAA 11158 contains three major sunspots (see Fig. 2). The western spot has positive polarity and the eastern one negative polarity. The flaring PIL is located in the central spot separating negative (north) from positive (south) polarity. The PIL runs along an alignment of umbral cores, i.e., the region is almost void of penumbral filaments. The nomenclature of umbral fine structures follows the definition in Sobotka, Bonet & Vazquez (1993). Basically, the active region is composed of two bipolar regions, which both appeared on 2011 February 11 and co-evolved with the result that the trailing spot of one region overlapped with the leading spot of the other region. The complex magnetic field topology of the central spot is the consequence of this interaction. We do not find any indications in the HMI magnetograms of narrow and elongated magnetic structures

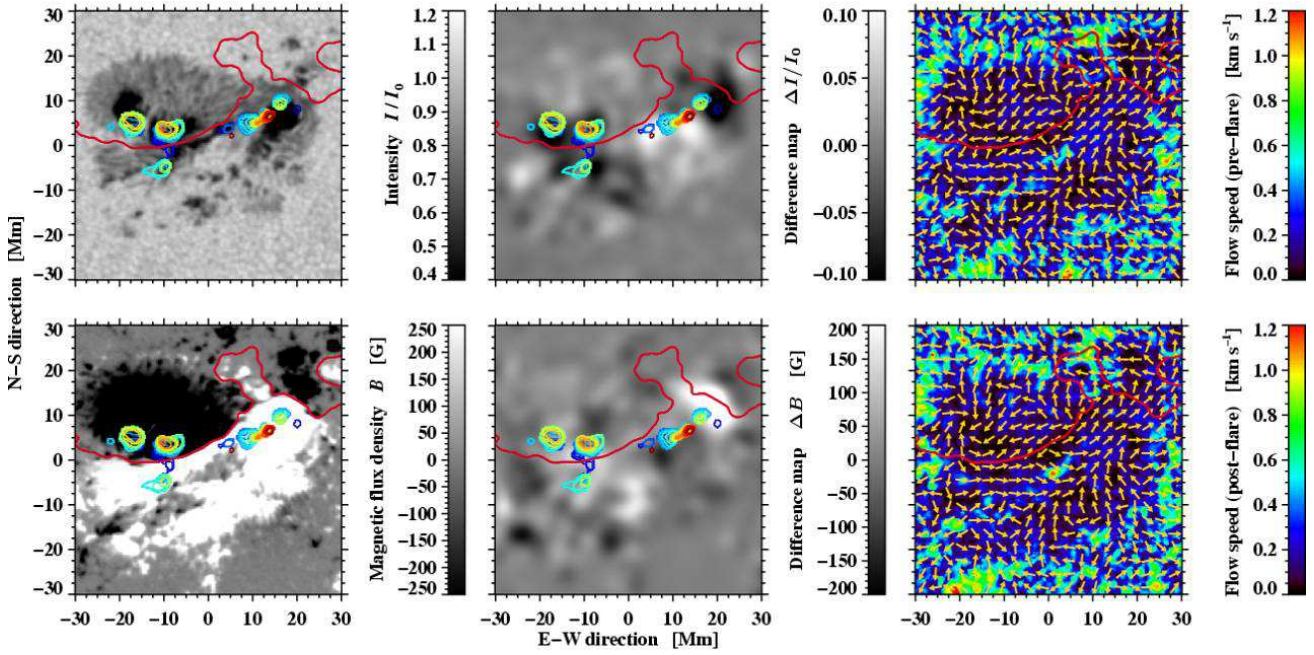


Fig. 4 ROI depicting the central region of active region NOAA 11158 where the X2.2 flare occurred. The *left* column shows a continuum image (*top*) and a magnetogram (*bottom*) at the peak of the flare (01:58 UT). The *middle* column contains difference maps (post- minus pre-flare phase) of the continuum intensity (*top*) and line-of-sight magnetic flux density (*bottom*), respectively. These maps were smoothed with a Gaussian (FWHM of 4.0 Mm) to emphasize regions of flare-induced changes in the photosphere. Superposed on all these maps are white-light flare kernels, which are depicted in the same way as in Fig. 2. Finally, the *right* column compares the horizontal flow *speeds* before (*top*) and after (*bottom*) the flare, respectively. The white circle encompasses a circular area of enhanced flow speed, which appeared after the flare. Orange arrows indicate the *direction* of the horizontal proper motions. The red curve in all panels refers to the flaring PIL.

along the flaring PIL, which were often observed in league with major solar flares (Wang *et al.* 2008; Zirin & Wang 1993). Such features are also absent in maps of the linear polarization for the pre- and post-flare phases (Wang *et al.* 2011). There, only an enhancement of the linear polarization is observed after the flare, which is indicative of an enhancement of the transverse magnetic fields along the PIL. Flare transients are visible in the magnetograms from 01:48–02:04 UT on both sides of the PIL, which are related to the two central flare kernels (see Figs. 2 and 3).

Before looking at flows, which are related to the X2.2 flare, we present an overview of the overall horizontal flow field within the active region. The average flow speed in regions covered by granulation is $424 \pm 55 \text{ m s}^{-1}$, where the standard deviation denotes the variation in the field-of-view (FOV) rather than a formal error. These values are in good agreement with Verma & Denker (2011) (see Tab. 3 therein) considering the image scale of $320 \text{ km pixel}^{-1}$. The values for the average flow speeds in penumbral and umbral regions are $159 \pm 11 \text{ m s}^{-1}$ and $117 \pm 5 \text{ m s}^{-1}$, respectively. These values are significantly lower than flow speeds previously derived from *Hinode* G-band images. However, considering the vast difference among active regions, they are still reasonable.

The moat flow is most prominent around the leading sunspot, where it extends about 10.0 Mm beyond the sunspot boundary. Typical flow speeds within the moat are

about 500 m s^{-1} but speeds in excess of 1.0 km s^{-1} are also commonly encountered. All other sunspots show indications of moat flow as well – in particular, when regular, well formed penumbrae exist with a radial filamentary structure. Using time-lapse continuum and magnetogram movies (e.g., Movie 1 in Schrijver *et al.* 2011) twisting motions become apparent in both the trailing and central spots. Spots with negative polarity turn counterclockwise, whereas a clockwise twist can be seen in the positive-polarity region of the central spot. In these locations, where penumbral filaments are no longer radially aligned, the moat flow is either suppressed or does not exist at all. This pattern is also imprinted on LCT maps and can be seen, when the flow vectors are visualized at high resolution. Furthermore, moving magnetic features (MMFs), which are tracers of the moat flow in magnetograms, follow these curved tracks as well.

Shear flows are difficult to detect in the flow maps depicted in Fig. 3, which encompass the entire active region. Therefore, we display zoomed-in versions of the pre- and post flare flow fields in the right column of Fig. 4. Since the flows near the PIL are very low (a few 100 m s^{-1}) and sometimes even lower than 100 m s^{-1} , we superposed arrows of equal length, which indicate the flow direction, on the horizontal speed maps. The low values of the shear flows could be explained by the larger image scale of HMI continuum images as compared to high-resolution *Hinode* G-band images. The PIL separates the larger umbral cores of negative

polarity to the north from the linear alignment of smaller umbral cores of positive polarity to the south. These umbral cores are only separated by a strong light-bridge, i.e., the intervening space is void of any penumbral fine structure. As a consequence, only very few contrast-rich features contribute to the speed measured by the LCT algorithm.

Shear flows are encountered along the strongest gradients of the PIL. In the pre-flare flow map, the PIL occupies in many location areas of zero flow speed, as expected for counter-streaming flows. After the flare, shear flows, which were originally associated with the positive magnetic polarity, extend more into the territory of negative polarity. This shift of the counter-streaming region towards the north is cospatial with the region of enhanced transverse fields reported by Wang et al. (2011). Another interesting post-flare flow feature is a small circular area of enhanced flows, which is marked by a white circle in the lower-right panel of Fig. 4. Here, the flow speed reaches up to 1.2 km s^{-1} . Small-scale brightenings are visible in the continuum images, which cross the void within the positive polarity from north to south. This motion is accompanied in magnetograms with fast traveling MMFs. The circular area of enhanced flows is in close proximity to a region of rapid penumbral decay. In a time-laps movie of HMI continuum images and magnetograms, the overall shear motions are very apparent leading to the impression that the flux system of opposite polarity are sliding along each other on both sides of the PIL.

As mentioned in Sect. 1, rapid penumbral decay and umbral strengthening are common photospheric phenomena after major solar flares. Difference maps for continuum and magnetograms are presented in the middle column of Fig. 4. All early flare kernels are located directly in an umbral core or in close proximity. These regions get darker after the flare and the magnetic flux density increases. Only for the flare kernel which lasted longest (dark red contours in Figs. 2 and 4), we find a decaying penumbral region in which the magnetic flux density diminishes. However, these flare-related changes are small compared to photospheric changes reported in the literature.

White-light emission was observed from the initiation of the flare (01:49 UT), through its peak time (01:54 UT as compared to 01:56 UT for the GOES X-ray flux in the 0.1–0.8 nm range shown in Fig. 1), until the emission faded away shortly thereafter (02:03 UT). At its maximum, the white-light flare emission covered an area of about 75 Mm^2 . The Gaussian smoothing results in flare kernels, which are somewhat larger and more contiguous than what can be seen in time-lapse movies of the original data. The time profile of the flare kernel contours matches well the Ca II H flare emission depicted in Fig. 1 of Wang et al. (2011).

All flare kernels are located at the border of umbral regions on both sides of the PIL. The first two flare kernels appear at the same time in the central sunspot near two umbral cores of negative polarity, which are separated by a strong light-bridge. The flare kernel to the east is very stable and

only slightly varies in size. The other flare kernel initially straddles the PIL and then moves towards the north. The other two flare kernels are located on the other side of the PIL in a region of positive magnetic flux. The western one shows rapid motion to the west. On average, the flare ribbons move with a speed of about 10 km s^{-1} and cover a distance of 5–12 Mm. Based on the continuum emission, the two-ribbon flare can be characterized as an X-type flare, where the eastern flare kernels are associated with the hard X-ray (50–100 keV) footpoints (see Fig. 1 in Wang et al. 2011). The connecting line of these X-ray footpoints is perpendicular to the PIL.

4 Discussion and conclusions

We have presented some exploratory work adapting the LCT algorithm of Verma & Denker (2011) to HMI continuum images. We were able to detect photospheric signatures of major solar flares in HMI data, e.g., rapid penumbral decay, umbral strengthening, shear flows, and white-light flare kernels. However, compared to previous studies, the phenomena are rather weak, which is rather surprising for a flare of this magnitude.

Counter-streaming motions along the PIL can contribute to the shear of magnetic field lines straddling the magnetic neutral line, thus contributing to the build-up of energy, which is then released during a flare (Deng et al. 2006; Denker et al. 2007; Liu et al. 2010; Yurchyshyn et al. 2006). The counter-streaming region, which was shifted towards the north after the flare, is cospatial with the area of enhanced transverse magnetic field identified by Wang et al. (2011). These authors take this enhancement as an indication of tether-cutting (Moore et al. 2001) at low atmospheric layers (see also Liu et al. 2010; Yurchyshyn et al. 2006). We conclude further that a rearrangement of the low-lying horizontal magnetic field can lead to an alteration of the horizontal flow field.

Another signature of such effects is the localized area with elevated horizontal proper motions near the PIL (white circle in Fig. 4), which might be an indication, that after stress relief within the magnetic field topology, shear motions along the PIL can increase again. This notion is also supported by the observation that the flow speed in the proximity of the PIL increases by about 5% after the flare. However, we should point out that these photospheric shear motions as measured by LCT are still rather small (cf., Deng et al. 2006; Yang et al. 2004). The low flow speeds for the shear motions could be attributed to a PIL, which is located between umbral cores so that only few features contribute to the LCT signal. In addition, the lower spatial resolution of HMI as compared to *Hinode* data might also increase the difficulty to extract these photospheric signatures. However, a comparison with high-spatial resolution *Hinode* data is beyond the scope of this research note.

Photospheric observations can only provide limited information about the magnetic field evolution above an ac-

tive region, since the restructuring of the coronal magnetic field is only weakly linked to changes of the photospheric magnetic field. Nowadays, EUV images of SDO's *Atmospheric Imaging Assembly* (AIA) and the two spacecrafts of the *Solar TERrestrial RELations Observatory* (STEREO) as well as coronagraph observations of STEREO and the *Solar and Heliospheric Observatory* (SoHO) provide a comprehensive three-dimensional picture of eruptive events in the corona. Based on data of these spacecrafts and instruments Schrijver et al. (2011) present a detailed account of coronal activity and dynamics related to the X2.2 flare in active region NOAA 11158, which include expanding loops above the PIL before the onset of the flare, an EIT wave (also seen as a Moreton wave in $H\alpha$), and an earth-directed halo CME with a speed of 900 km s^{-1} . The authors interpret the observations supported by MHD modeling as an expanding volume, where a warming compression front moves in advance of the erupting flux rope.

Interestingly, no $H\alpha$ filament was observed as often found in the core of an erupting flux rope. Even though filament channels correspond to a state of maximum magnetic shear (Martin 1998), gradual changes and slowly moving opposite magnetic elements are a prerequisite for a stable filament. In contrast, small-scale, rapidly changing magnetic fields are not favorable for filament formation. Thus, the strong shear motion of two opposite polarity sunspot groups sliding past each other might have prevented the formation of a filament.

Only diminutive white-light flare kernels were observed for the X2.2 flare in active region NOAA 11158 (cf., Fig. 3 in Xu et al. 2004). The flare kernels to the west on both sides of the PIL were closely related to the hard X-ray emission. Such a close spatial relationship was also found by Krucker et al. (2011) between hard X-ray and G-band flare kernels. Considering the spatial resolution of HMI data and the image processing techniques used to extract the flare kernels with sizes of 2–5 Mm, our results are compatible with their high-resolution G-band observations, which show fine structures in flares even below 1 Mm. The altitude of the flare continuum emission is still debated. However, in transition region SDO/AIA 160 nm filtergrams and chromospheric *Hinode* Ca II H images well-defined J-shaped ribbons extend much further along both sides of the PIL. Potts et al. (2010) used a simplified radiative transfer model to explain such observations in the context of the “thick-target” model (Hudson 1972) assuming that high-energy electrons in the 10–100 keV range are responsible for the white-light flare emission in an optically thin, excited region with temperatures of about 10^4 K some 750–1300 km above the photosphere.

Acknowledgements. SDO/HMI data are provided by the *Joint Science Operations Center – Science Data Processing*. The GOES X-ray flux measurements were made available by the *National Geophysical Data Center*. MV expresses her gratitude for the generous financial support by the *German Academic Exchange Service* (DAAD) in the form of a PhD scholarship. LB's research internship in Germany was made possible by DAAD's *Research Intern-*

ships in Science and Engineering program. CD was supported by grant DE 787/3-1 of the German Science Foundation (DFG). The authors would like to thank Drs. Horst Balthasar and Haimin Wang for carefully reading the manuscript and providing ideas, which significantly enhanced the paper.

References

- Battaglia, M., Kontar, E.P.: 2011, ArXiv e-prints, 1107.3808
- Chae, J., Sakurai, T.: 2008, ApJ 689, 593
- Couvidat, S., Schou, J., Shine, R.A., et al.: 2011, Sol. Phys., DOI: 10.1007/s11207-011-9723-8
- Deng, N., Xu, Y., Yang, G., et al.: 2006, ApJ 644, 1278
- Denker, C., Johannesson, A., Marquette, W., et al.: 1999, Sol. Phys. 184, 87
- Denker, C., Deng, N., Tritschler, A., Yurchyshyn, V.: 2007, Sol. Phys. 245, 219
- Gosain, S., Venkatakrishnan, P., Tiwari, S.K.: 2009, ApJ 706, L240
- Harvey, K.L., Harvey, J.W.: 1976, Sol. Phys. 47, 233
- Hudson, H.S.: 1972, Sol. Phys. 24, 414
- Kubo, M., Yokoyama, T., Katsukawa, Y., et al.: 2007, PASJ 59, 779
- Krucker, S., Hudson, H.S., Jeffrey, N.L.S., et al.: 2011, ApJ 739, 96
- Liu, C., Deng, N., Liu, Y., et al.: 2005, ApJ 622, 722
- Liu, R., Liu, C., Wang, S., et al.: 2010, ApJL 725, L84
- Martin, S.F.: 1998, Sol. Phys. 182, 107
- Martínez Oliveros, J.C., Couvidat, S., Schou, J., et al.: 2011, Sol. Phys. 269, 269
- Maurya, R.A., Reddy, V., Ambastha, A.: 2011, ArXiv e-prints, 1106.4166
- Moore, R.L., Sterling, A.C., Hudson, H.S., Lemen, J.R.: 2001, ApJ 552, 833
- November, L.J., Simon, G.W.: 1988, ApJ 333, 427
- Potts, H.E., Barrett, R.K., Diver, D.A.: 2004, A&A 424, 253
- Potts, H., Hudson, H., Fletcher, L., Diver, D.: 2010, ApJ 722, 1514
- Schou, J., Borrero, J.M., Norton, A.A., et al.: 2010, Sol. Phys., DOI: 10.1007/s11207-010-9639-8
- Schrijver, C.J., Aulanier, G., Title, A.M., et al.: 2011, ApJ 738, 167
- Schuck, P.W.: 2006, ApJ 646, 1358
- Sobotka, M., Bonet, J.A., Vazquez, M.: 1993, ApJ 415, 832
- Sudol, J.J., Harvey, J.W.: 2005, ApJ 635, 647
- Tan, C., Chen, P.F., Abramenko, V., Wang, H.: 2009, ApJ 690, 1820
- Verma, M., Denker, C.: 2011, A&A 529, A153
- Wachter, R., Schou, J., Rabello-Soares, M.C., et al.: 2011, Sol. Phys., DOI: 10.1007/s11207-011-9709-6
- Wang, H., Spirock, T.J., Qiu, J., et al.: 2002, ApJ 576, 497
- Wang, H., Jing, J., Tan, C., et al.: 2008, ApJ 687, 658
- Wang, S., Liu, C., Liu, R., et al.: 2011, ArXiv e-prints, 1103.0027
- Welsch, B.T., Abbett, W.P., De Rosa, M.L., et al.: 2007, ApJ 670, 1434
- Xu, Y., Cao, W., Liu, C., et al.: 2004, ApJ 607, L131
- Yang, G., Xu, Y., Cao, W., et al.: 2004, ApJ 617, L151
- Yurchyshyn, V., Liu, C., Abramenko, V., Krall, J.: 2006, Sol. Phys. 239, 317
- Zirin, H., Wang, H.: 1993, Nature 363, 426